Title

A reduced model for edge localized mode control by supersonic molecular beam injection and pellet injection

Journal

Physics of Plasmas, 27(7)

ISSN

1070-664X

Authors

Rhee, T
Kwon, Jae-Min
Diamond, PH

Publication Date

2020-07-01

DOI

10.1063/5.0009583

Peer reviewed

A reduced model for edge localized mode control by supersonic molecular beam injection and pellet injection

T. Rhee,[1, a)] Jae-Min Kwon,[1] and P.H. Diamond[2]

[1)] *NFRI, 169-148, Yuseong-gu, Daejeon 34133, Republic of Korea*

[2)] *CMTFO and CASS, UCSD, 9500, Gilman Dr. La Jolla, CA 92093, USA*

We develop a diffusive, bistable, tri-unstable cellular automata(CA) model to study the dynamics of H-mode pedestal with edge localized modes(ELMs), and their control by supersonic molecular beam injection(SMBI) and pellet injection(PI). It is shown that the new CA model can reproduce the key features of H-mode pedestals with various types of ELM, including Type-I ELM. SMBI and PI are modeled as additional grain injections into pedestal with varying degrees of injected materials and profiles. It is found that H-mode pedestal responds to SMBI differently depending on the baseline fueling. If the baseline fueling is large enough to allow Type-I ELM, SMBI enhances large transport avalanches caused by ballooning instabilities. These avalanches prevent the total pedestal current from reaching the boundary for peeling instability. On the other hand, if the baseline fueling is low to avoid Type-I ELM, SMBI enhances small scale avalanches, which prevent the pedestal from growing to profiles globally vulnerable to ballooning instabilities. These imply that SMBI can mitigate different types of ELM by converting them to more benign types. From CA modeling of pellet injection, it is shown that Type-I ELM can be triggered by pellet injection with sufficient strength and depth. Scanning the frequency of pellet injection, it is found that a maximum efficiency of pellet pacing is achieved when the injection frequency is approximately ten times of the natural frequency of Type-I ELM.

[a)] trhee@nfri.re.kr

I. INTRODUCTION

Edge localized modes (ELMs) are violent relaxation event occurring in H-mode pedestal[1]. Inducing bursty release of stored energy in the pedestal, ELMs also serve as transport channels for particles, momentum, and impurities. Regarding the operation of H-mode plasma, ELMs have multiple facets. ELMs degrade plasma performance by reducing pedestal pressure. Also, they can damage plasma facing component(PFC) by excessive heat loads. On the other hand, ELMs can contribute to the enhancement of plasma performance by preventing the accumulation of high-Z impurities. Therefore, it is important to understand the physics of ELMs and also develop methods to control them.

Along with extensive theoretical and experimental studies on ELM physics, great experimental efforts aim to develop reliable ELM control methods. To prevent pedestal pressure from growing to the threshold for large peeling-ballooning instabilities, various external actuators are employed to increase transport in H-mode pedestal. Resonant magnetic perturbation(RMP) is one of the actuators with which extensive researches is on-going[2–5]. This approach exploits magnetic field ergodization near the pedestal top by an external magnetic field perturbation[6]. Another type of the actuator for ELM control employs localized fueling methods such as supersonic molecular beam injection(SMBI) or pellet injection(PI).

Recently, SMBI was tested for ELM control on HL-2A[7–9], KSTAR[8,10], and EAST[11]. The experimental results from these devices revealed common characteristics of ELM mitigation by SMBI, which can be summarized as follows.

- Neutrals from SMBI are deposited mainly in H-mode pedestal foot.
- The slope of plasma density profile in the pedestal decreases due to SMBI.
- The influence time τ_I defined as the duration of ELM mitigation by SMBI, shows a strong correlation with the particle confinement time τ_p. This implies that the mechanism of ELM mitigation is related to particle transport.
- During the τ_I, the high frequency components of the particle flux and density fluctuation intensity are enhanced.

In the EAST experiments[11], it was found that the increase of high frequency components are related to the appearance of intermittent, small scale turbulence during the τ_I.

ELM control by PI aims to increase the ELM frequency f_{ELM}. In the steady state, energy loss by a ELM ΔW_{ELM} is proportional to $1/f_{ELM}$. By synchronizing f_{ELM} with the higher PI frequency f_{PI} than normal f_{ELM}, the energy loss by triggered ELM is expected to be reduced. For ITER as an example the required value of f_{PI} allowing an endurable level of ΔW_{ELM} is about $10 \sim 30 f_{ELM}$. From ELM pacing experiments on ASDEX-U[12–14], the following results were obtained.

- PI triggers ELM with shorter-term MHD activity than those for nominal ELMs.
- ELMs synchronize with PI, up to $f_{PI} \sim 3 f_{ELM}$.
- ΔW_{ELM} is reduced to $\sim 1/f_{PI}$, as expected.

The experiments on DIII-D[15] achieved an ELM pacing up to $f_{PI} \sim 10 f_{ELM}$.

As localized fueling methods, SMBI and PI are considered as potentially important tools for various aspects of tokamak operation including ELM control. It is crucial to develop theoretical models to describe their impact on the H-mode pedestal. In this context, we would like to note that there have been great progresses in the MHD simulations of ELM and related phenomena. However, due to great complexity of the physics involved in the H-mode pedestal and ELM, there are still many limitations in the approaches based on conventional MHD simulations. We would like to note that it is beyond the capability of the conventional approaches to simulate the dynamics of H-mode pedestal on a time scale, which is long enough to study the statistical properties of H-mode pedestal under many SMBIs or PIs. Thus tractable reduced models retaining key physical elements of related phenomena are required to complement the conventional approaches in understanding ELM control experiments.

The simplest model describing ELMy H-mode plasmas is the cellular automata (CA), based on a bi-stable automata rule[16,17]. The bi-stable CA rules employed in Ref. 16–18 model transport by micro-turbulences and ballooning type MHD instabilities, which are driven by the local pressure gradient and its local relaxation. It was shown that the bi-stable CA model captures the key features of edge transport bifurcation, the dynamics of H-mode pedestal, and ELM like avalanches triggered by the local pressure gradient limit etc. The observed avalanche type pedestal collapse have many features in common with the pressure-driven Type-II/III ELMs in H-mode experiments.

The bi-stable CA model was extended to model SMBI and study the impact of SMBI on transport avalanches spanning whole H-mode pedestal in Ref. 18. Employing the extended CA model, the study investigated how SMBI can affect Type-II/III ELMs. The key results can be summarized as follows[18]:

- If the strength of perturbation induced by SMBI is within a proper range, SMBI increases the intensity of small scale fluctuations and the resulting transport. They release the pedestal pressure and prevent the pedestal gradient from growing to the point of vulnerability to large scale Type II/III ELMs.

- There is a limit on the penetration depth of SMBI for ELM mitigation. As the penetration depth becomes deeper, the release of pedestal pressure by SMBI becomes less efficient. Eventually large scale ELMs are triggered by SMBI, which are similar with ELM pacing by PI.

- The physical mechanisms for the ELM mitigation by SMBI are different from those for the ELM pacing by PI. SMBI promotes the self-organization of H-mode pedestal by small scale transport to avoid global pressure-driven instabilities.

Though the model is highly simplified, it provides a useful picture to understand ELM mitigation experiments using SMBI[8,9,11]. However, in describing broader aspects of ELM phenomena, the CA models in Refs. 16–18 have limitations. It is due to the absence of rules encompassing peeling instabilities critical to Type-I ELM. A Type-I ELM is destabilized by peeling-ballooning instability driven by combination of pedestal current and pedestal pressure gradient ∇P.[19] To model transport by Type-I ELMs, we need to extend the rule to trigger global pedestal transport events by current in the H-mode pedestal.

In this paper, we extend the CA model presented in Ref. 18 to include peeling mode type relaxation events. Since bootstrap current driven by steep pressure gradient dominates the total current in the H-mode pedestal, the pedestal current can be approximated as proportional to total pedestal pressure. The latter can be calculated by integrating the grains in the pedestal. Then, by introducing a rule which discharges excess current(i.e. pressure) above a critical level, transports induced by Type-I ELM can be incorporated into the CA model. This extended model will be described in the Sec. II with the illustration in the Fig. 1. Once the model is extended, we can study the dynamics of ELMs with SMBI or

PI in wider ranges of H-mode plasma conditions. Using the extended model, in this work, we aim to study the impact of SMBI and PI on H-mode pedestals where various types of ELMs are present.

The remainder of this paper is organized as follows. In Sec. II, the extended CA model which includes pedestal height effects is presented. Employing the extended model, the dynamics of the H-mode pedestal including various types of ELMs are studied in Sec. III. The physical mechanisms of ELM mitigation by SMBI are investigated in Sec. IV. SMBI parameters are varied to find an optimal injection condition for ELM mitigation. In Sec. V, PI is studied to find an optimal condition for pellet pacing of Type-I ELM. Finally, summary and discussion are given in Sec. VI.

II. MODEL

In Ref. 16, a basic CA model was proposed to describe the dynamics of H-mode pedestal. The CA rules in the model can be summarized as follows. The radial domain is discretized as cells, and each cell is occupied by a finite number of grains H_i (i denotes the radial index of the cells). We provide a constant fueling of grains N_F in every time steps, which reflects the external heating to achieve and sustain H-mode state in real experiment. In this one dimensional CA model, the left boundary ($i = 1$) is closed and grains are only ejected through the right boundary ($i = 100$). Transport by plasma turbulence is represented as a collection of localized flips of grains (D_z) from cell to adjacent cell. The flipping of grains occurs when the gradient $Z_i \equiv H_i - H_{i+1}$ exceeds a certain limit Z_{c1} as $Z_i > Z_{c1}$. Turbulence suppression by diamagnetic $E \times B$ flows is modeled by introducing a second threshold for the gradient $Z_{c2}(> Z_{c1})$. For the slope window $Z_{C3} > Z_i > Z_{C2}$, where Z_{C3} is the third critical limit described in the following paragraph, the transport of grains by turbulence and MHD instability is suppressed. Neoclassical diffusion is implemented as a baseline transport process with coefficient D_N. Therefore, it serves the role of transport even when the flipping and toppling are suppressed. When N_F exceeds a certain critical value, an $L \rightarrow H$ transition occurs and H-mode pedestal is formed[16].

The CA rules apply a hard limit $Z_{c3}(> Z_{c2})$ on local gradients to model the excitation of ballooning instabilities (i.e. ∇P limit). When a local gradient hits this MHD hard limit $Z_i > Z_{c3}$, an amount of grains $1 + (Z_i - Z_{c1})/2$ are toppled or mixed into a neighboring

cell. Thus this process relieves a gradient exceeding the hard limit to a value above Z_{c1}. This model provides rules for the spatio-temporal evolution of grains, which manifest quasi-periodic ELM-like ejection events, composed of toppling avalanches spanning the whole H-mode pedestal.

In Ref. 18, the CA model was extended to include SMBI as additional grain injection(AGI). A single SMBI was modeled as continuous injection of grains during a given time interval. AGIs with various combinations of temporal duration and spatial location were tested to find an optimal injection scheme for ELM mitigation by SMBI.

To include transport by peeling instabilities in the CA model, we need to implement a new CA rule tied to total (not local) pedestal current. In the H-mode pedestal with steep pressure gradient, the current is dominated by the pressure driven bootstrap current, which is proportional to the pressure gradient $j_{bs} \propto dP/dr$. So we can estimate the total current in the pedestal as

$$j_{tot}^{ped} \propto \int_{r0}^{r1} \frac{dP}{dr} dr \propto H_{ped}^{top}. \tag{1}$$

With the rule to evaluate the pedestal current, we introduce a new limit H_c^{top} on the total current to model transport by peeling instabilities. The total current represented by H_{ped}^{top} fluctuates due to the flipping and toppling for transports by micro-turbulence and ballooning instability. We choose a time interval ΔT_P to calculate averaged pedestal height $\langle H_{ped}^{top} \rangle$ corresponding to the averaged total current. If the averaged total current exceeds the limit $\langle H_{ped}^{top} \rangle > H_c^{top}$, a number of grains ΔN_{ped} are expelled from the pedestal. The number ΔN_{ped} is set to match typical values for the loss of pedestal pressure due to Type-I ELM, *i.e.* $\Delta N_{ped}/N_{ped}^{tot} = 0.1$. Here, N_{ped}^{tot} denotes the number of total grains in the pedestal. In removing the grains, we keep the local gradients across the pedestal at the same values before the removal. The cartoon in Fig. 1 demonstrates this procedure. With this additional rule, for global peeling instabilities, the new CA model exhibits the characteristics of H-mode with Type-I ELMs. These results will be presented in great details in the next section.

To model PI in addition to SMBI, we also extend the AGI scheme in Ref. 18. Comparing SMBI and PI, SMBIs tend to yield longer injection duration of a few ms, while PIs have shorter time duration of tens of μs. The deposition profiles from SMBIs tend to take shallower forms centered around the base of the H-mode pedestal[8], while those from PIs are more controllable and the resulting penetration can be beyond the pedestal top[13,15]. It is

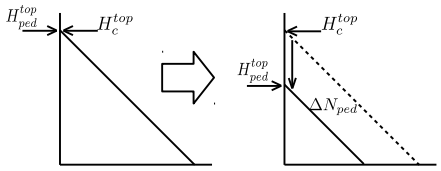

FIG. 1. The schematics of transport by peeling instabilities.

noteworthy that both methods deposit similar numbers of deuterium molecules $\sim 10^{20}$ D_2 into tokamak plasma. We set the duration and amplitude of injections for SMBI and PI as Fig. 2. The AGI for PI is set with a larger amplitude and a shorter duration as compared to AGI for SMBI. In this work, we employ Gaussian deposition profiles with various sizes and locations to study the effects of SMBI and PI operation parameters on ELM control. Figure 3 compares the typical form of SMBI and PI profile used in this work.

In real experiments, both SMBI and PI deposition profile are not axisymmetric. For pellet injection, toroidally localized thermalization of ions was suggested during ELM triggering[20]. For simplicity, the CA model utilizes toroidally averaged profiles as presented in Fig. 3.

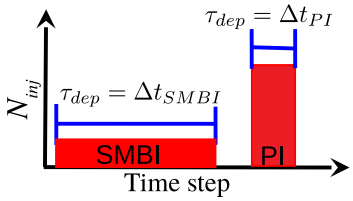

FIG. 2. The AGI models for SMBI and PI. The Left and right rectangle are for SMBI and PI respectively.

SMBI and PI affect various physical processes leading to ELM burst. In the CA model, this implies that the rules for the criticality and transport can be changed by the injections. However, putting those details into the model is beyond the scope of this work, and we employ the same rules to trigger ELM for both natural ELM and induced one by SMBI and PI.

Table I summarizes the key elements and rules of the extended CA model and their correspondence with H-mode pedestal physics.

The simulation parameters for the extend CA model are chosen as $Z_{c1} = 8$, $Z_{c2} = 20$, $Z_{c3} = 30$, and $H_c^{top} = 2100$. The baseline diffusion coefficient is set as $D_N = 0.08$ and the

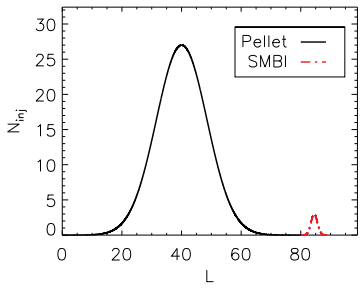

FIG. 3. Typical deposition profiles of pellet (the black solid curve centered at $L = 40$) and SMBI (the red dash-dot curve centered at $L = 85$).

TABLE I. Analogy between tokamak transport model and cellular automata model

Transport mechanism	**Automata rules**
Critical gradient range for micro-turbulence	Unstable range of slope
Moderate local eddy-induced transport	Flipping of fixed number of grains
Flow shear suppression of turbulence	Steep range of slope above the unstable range
Critical gradient for ∇P driven MHD event	Hard limit on slope
Transport by ∇P driven MHD event	Toppling of grains
Critical current for peeling instabilities	Hard limit on the height of pedestal top
Transport by peeling instabilities	Removal of whole excessive grains from pedestal
Plasma contents	**Cellular Automata quantity**
Localized fluctuation(eddy)	Grid site(cell)
Total energy/particle content	Total number of grains (total mass)
Heating noise/background fluctuations	Random input of grains
Energy/particle flux	Grain flux
Mean temperature/density profiles	Average slope of system
Transport event	Avalanche

amount of grain flipping for turbulent transport is chosen as $D_Z = 3$. For the calculation of the averaged pedestal height, we set $\Delta T_P = 20$. The total simulation time is set as 3×10^5 for typical runs. But for cases requiring statistical analysis, the simulation is continued up to 1×10^6.

With the given critical gradients and transport values, the system exhibits different behavior for varying N_F.[16,17] For weak fueling rates less than the flipping rate $N_F < 3$, the system shows L mode like features. In this range the slope of the system is less than Z_{c1} and turbulence transport (i.e. flipping) is dominant. If the fueling rate is higher than the flip-

ping $N_F > 3$, the system exhibits H-mode like features with slope $Z_i > Z_{c1}$. Since the slope between Z_{c1} and Z_{c2} prohibits turbulent transport, a pedestal structure is formed. The slope increases continuously until it reaches Z_{c2} and avalanches are triggered by ballooning instabilities in the pedestal. Further increase of fueling will trigger various phenomena controlled by Z_{c3} and the details will be investigated in Sec. III.

III. ELMY H-MODE PEDESTAL WITH PEELING-BALLOONING INSTABILITIES

Employing the extended CA model, we can reproduce the key features of H-mode pedestals with various types of ELMs. If we choose $N_F > 10$, which is 3 times higher than the threshold for the $L \to H$ transition in the chosen set of parameters, an H-mode pedestal is formed and large ELMs appear. Figure 4 shows the evolution of the pedestal between two large ELMs triggered by peeling instabilities at $t \approx 300$ and $t \approx 4600$ in the case with $N_F = 12$. The inter-ELM period can be categorized into two different phases, as indicated by the dashed vertical lines in Fig. 4(b). In the first phase marked as $P1$ in the Fig. 4(b), right after the first big ELM shown as the blue vertical line in the Fig. 4(a), the pressure values near the pedestal bottom ($i = 85 - 100$) drop significantly and their gradients become lower than the ballooning limit. Therefore, in this phase, the pedestal is dominated by turbulent transport(the black regions) and $E \times B$ stabilization(the red regions), with a rapid recovery of the total pressure. Steep gradients also develop during this phase.

In the second phase marked as $P2$ in the Fig. 4(b), transport avalanches triggered by ballooning instabilities appear and strongly regulate the pedestal gradients. A single avalanche corresponds to a single green triangle appearing in the spatio-temporal evolutions of grains. If the number of fueling grains N_F is smaller than the number of grains ejected by the transport avalanches, the pedestal is constrained to stay below the criterion for peeling instabilities, thus to avoid Type-I ELMs. However, if the fueling is sufficiently strong to overcome the transport avalanches ($N_F > 10$ for our set of parameters), the pedestal top H_{ped}^{top} gradually rises to the peeling limit H_c^{top}. The global pedestal crash (the blue vertical line) then reappears, as shown in Fig. 4(a). This Type-I ELM cycle appears repeatedly as the simulation is proceeding.

Figure 5 shows the detailed temporal evolution of the pedestal profile during an ELM

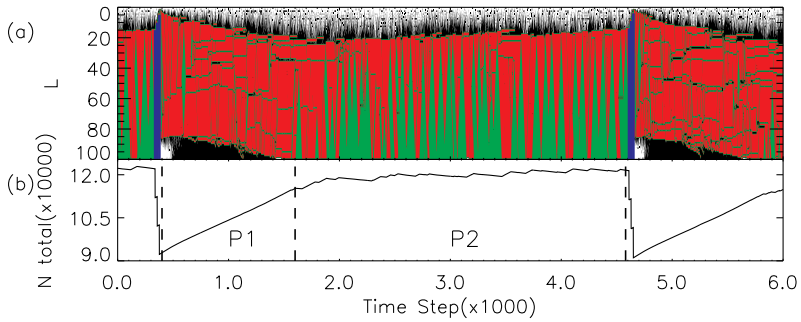

FIG. 4. Characteristics of ELM cycle. (a) shows the evolutions of cell status with different colors: the white and black cells represent stable and turbulent cells, respectively. The red cells represent $E \times B$ stabilized region. The green and blue cells imply the triggering of ballooning and peeling instabilities, respectively. (b) shows the evolution of the total number of grains in the pedestal.

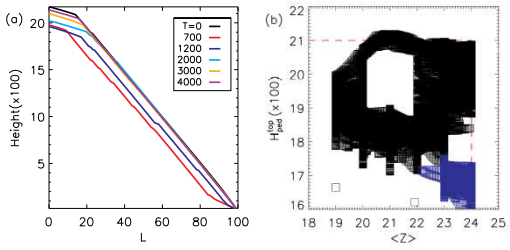

FIG. 5. The evolution of pedestal during ELM cycles: (a) pedestal profiles in different time steps during a type-I ELM crash, (b) corresponding pedestal top vs averaged pedestal gradient $\overline{Z} \equiv \langle Z_i \rangle$ (i.e. total bootstrap current vs averaged ∇P). In figure (a), $T = 0$ corresponds to the time right before the ELM crash (i.e. about the ELM crash timing). $T = 4000$ corresponds to the time after 4000 time steps after the crash. In figure (b), the black and blue squares represent the phase space evolutions of type-I and type-II/III ELM, respectively.

cycle. The initial ELM crash lowers both the pedestal top and the averaged pedestal gradient $\langle Z \rangle$ as the red curve ($T = 700$) in the Fig. 5(a) shows. The transport induced by peeling instability reduces the height of pedestal by ejecting grains uniformly. The overall gradient does not change by the transport. After this, localized transports induced by turbulence and ballooning instability follow and regulate the pedestal gradient. Since the fueling is continuously made, during the recovery phase of the pedestal, the average gradient increases rapidly with a rather mild increase of the pedestal top until the gradient reaches the ballooning limit $\overline{Z} = 24$. Then, the rapid increase of the pedestal height (i.e. the boot-

strap current) follows until it reaches the peeling limit (the horizontal red dashed line in Fig. 5(b)). This completes an ELM cycle in the counter-clock wise direction. The black boxes in Fig. 5(b) show these cycles for multiple Type-I ELMs. Below the threshold for Type-I ELM and above the LH-transition threshold, *i.e.* $4 \leq N_F \leq 10$, only Type-II or Type-III ELM appear. As an example, for $N_F = 5$, the corresponding ELM cycles are presented as the smaller blue boxes in Fig. 5(b). The cycles are bounded by the vertical line $\overline{Z} = 24$ and do not evolve to reach the peeling boundary for a Type-I ELM i.e. the horizontal red dashed line $H_{ped}^{top} = 2100$ in the figure. Thus we have two distinctive intervals of N_F for different types of ELM: $4 \leq N_F \leq 10$ for Type-II or Type-III ELM, and $N_F > 10$ for Type-I ELM.

In tokamak experiment, one way to identify Type-I ELM is to check the increase of ELM frequency for increasing heating power. It is an interesting test to check whether the big crashes triggered by the CA rule for peeling instabilities exhibit a similar trend. In the CA model, increasing power corresponds to stronger drive by higher N_F. Figure 6 shows the variation of large ELM frequency for increasing N_F. Indeed, it is clear that once N_F reaches the threshold for the peeling instabilities, ELM frequency increases for increasing N_F as expected for Type-I ELM.

It should be noted that ballooning instabilities always appear in the CA simulations of H-mode pedestal. However, the characteristics of ballooning instabilities and resulting transport avalanches change, depending on the existence of Type-I ELM. There are notable changes in the statistics of the avalanche size. The size of avalanche is represented by the duration of an avalanche event since an avalanche event continues until all pedestal gradients are lower than the hard limit. Figure 7 shows the variations of the duration [(a)] and the occurrence period [(b)] of avalanche events. Without peeling instabilities (i.e. Type-I ELMs), the duration of the avalanche events increases as N_F increases beyond the LH-transition threshold $N_F = 4$. The period of the avalanches decreases as the duration becomes longer for increasing N_F. These imply that the avalanches become larger and more frequent as N_F increases if we exclude Type-I ELM in the CA model.

With the inclusion of peeling instabilities, these trends change. Now, there are two mechanisms which can globally release pedestal pressure. Since Type-I ELMs appear more frequently for increasing N_F, global transport induced by Type-I ELMs becomes more significant in releasing pedestal pressure. As the pedestal pressure is primarily regulated by Type-I ELMs, the avalanches triggered by ballooning instabilities become less prominent,

and their duration and period saturate for the increasing N_F.

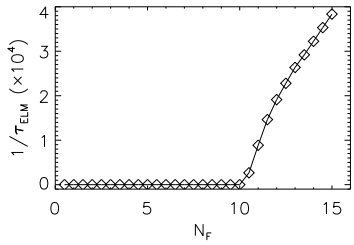

FIG. 6. The change of the frequency of large ELM for increasing fueling rate N_F.

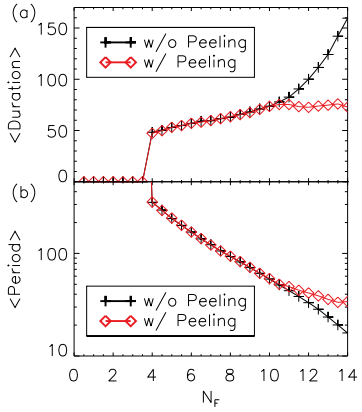

FIG. 7. The changes of the averaged (a) duration(size) and (b) period of transport avalanches triggered by ballooning instabilities for increasing fueling rate N_F. The black and red curves are for without and with transport rule by peeling instabilities, respectively.

IV. ELM MITIGATION BY SMBI

As explained in Sec. II, we model SMBI as AGI into H-mode pedestal. The amount of injected grains N_{inj}^{SMBI} can be set based on the ratio $N_{inj}^{SMBI}\Delta t_{SMBI}/N_{ped} = 2.2\%$ from experiments. Periodic SMBI pulses are injected into an H-mode pedestal with Type-I ELMs. The duration of a single SMBI is set as $\Delta t_{SMBI} = 400$ *i.e.* grains are injected continuously over the time interval $[t, t + \Delta t_{SMBI}]$. Here we set $N_F = 11$ and the ELM period is $\tau_{ELM} = 10^4$. The injection locations are near the bottom centered at $i = 95$. We find that after the

SMBI injection, the periodic collapses of the pedestal by Type-I ELMs disappears. Only transport avalanches triggered by ballooning instabilities shown as the green regions in Fig. 8(a) appear and regulate the pedestal. This can be interpreted as ELM mitigation by SMBI *i.e.* Type-I ELMs are replaced by smaller and more irregular transport events corresponding to Type-II or Type-III ELMs.

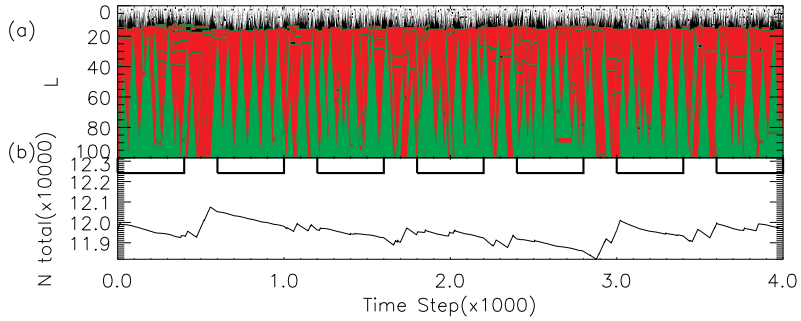

FIG. 8. (a) The changes of the pedestal evolution by SMBI and (b) the evolution of the total number of grains in the pedestal. Black rectangles in the top of (b) represent the intervals for SMBIs.

It should be noted that without SMBI, transport avalanches by ballooning instabilities also appear in between Type-I ELMs. However, there are statistical differences between the avalanches from the case with SMBI and those from the case without SMBI. Intensified green triangles during a SMBI [in Fig. 8(a)] implies that there are continuous toppling events triggered by local gradients which exceed the hard limit. Figure 9 compares the distribution of the duration of transport avalanches from the two cases (i.e. with and without SMBI) to verify the change of an avalanche size. It is clear that, if Type-I ELMs are suppressed by SMBI, avalanches become bigger and less frequent than those from the case with Type-I ELMs (i.e. without SMBI).

The changes of transport avalanches by SMBI depend on the level of N_F driving the pedestal. If we apply SMBI on H-mode pedestal without Type-I ELMs, which can be achieved by lower drives, different trends appear on the changes of the avalanches. Figure 9(a) shows the distribution of the avalanche duration times when we set $N_F = 5$ to avoid Type-I ELMs. Here, the red(triangle) and black(rectangle) curve denote the case with and without SMBI, respectively. As SMBI is applied, it is clear that the transport avalanches

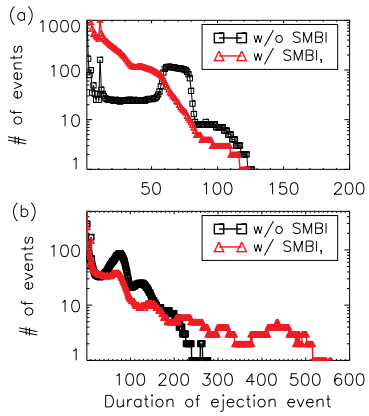

FIG. 9. The distributions of avalanche sizes in the case with(the red triangle) and without(the black rectangle) SMBI for (a) $N_F = 5$ and (b) $N_F = 11$. It should be noted that the scales of axes of (a) and (b) are different.

appear more frequently with smaller sizes. This can be interpreted as a mitigation of Type-II/III ELMs by SMBI, and the results are consistent with those in Ref. 18. We'd like to emphasize that this trend of avalanche changes for $N_F = 5$ is opposite to the trend for the stronger drive $N_F = 11$ [see Fig. 9(b)].

The different trends depending upon the drive N_F can be understood as follows. Additional grains from SMBI affect the H-mode pedestal in two ways. Firstly, they perturb the pedestal and change the spatio-temporal structure of transport events caused by ballooning instabilities. Secondly, they act as a drive to the pedestal, in addition to the baseline drive N_F. When the baseline drive is weak and SMBI is applied at the bottom of the pedestal, the first effect becomes prominent while the second one is minimized. These result in the fragmentation of global transport avalanches into smaller ones, *i.e.* the mitigation of Type-II/III ELMs[18]. However, if the baseline drive N_F is strong, the second effect becomes more important. SMBI drives the pedestal further, and global transport avalanches become bigger and less frequent as Fig. 9(b) shows.

When the baseline drive is strong enough to induce Type-I ELMs, SMBI enhances transport avalanches by making them bigger, which prevents the total current from reaching the critical value to trigger peeling instabilities. Figure 10 compares the evolutions of the

total current in the case with SMBI (the red solid curve) and without SMBI (the black solid curve). Without SMBI, the total current periodically reaches the critical value, so the pedestal undergoes periodic collapse. With SMBI, on the other hand, the total current is kept below the critical value. Comparing the averaged current and pressure of the two cases in Fig. 11(a), the case with SMBI has higher values due to the absence of Type-I ELM.

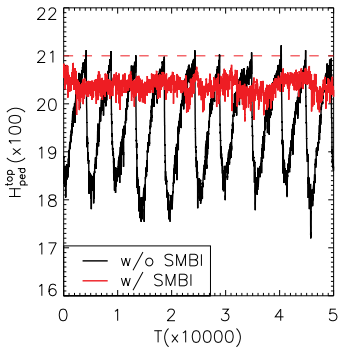

FIG. 10. The evolution of the height of the pedestal top with (the red solid curve) and without (the black solid curve) SMBI. The red dashed line indicates H_c^{top}.

Figure 11(b) shows the structural changes of the pedestal by SMBI. Comparing the averaged gradient near the region of SMBI deposition at $L = 80 - 90$, the case with SMBI shows higher values than the case without SMBI. The averaged gradient inner pedestal than deposition region ($L = 50 - 80$) shows an opposite trend *i.e.* the case with SMBI shows lower values than the case without SMBI.

Along with the enhancement of global avalanches spanning the whole pedestal, localized transport events with high frequencies also increase. Figure 12 compares the spectra of pressure oscillations near the pedestal bottom. Without SMBI (the black rectangle curve), the spectrum is dominated by low frequency components ($f < 10^{-3}$), which correspond to the frequencies of Type-I ELMs. With SMBI (the red triangle curve), these low frequency components disappear. But high frequency components (those with frequencies higher than 10^{-2}) increase and the spectrum develops a fat tail. The power of the fat tail is one order higher than the power of the spectral tail without SMBI. These imply that Type-I ELMs and resulting big transport events are replaced with Type-II/III ELMs and smaller transport

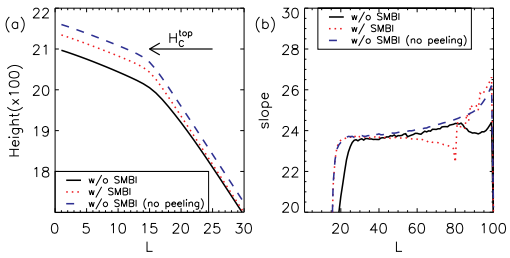

FIG. 11. The averaged (a) height and (b) slope of the pedestal with(the red dotted), without(the black solid) SMBI. The blue dashed line is the case without SMBI nor peeling instability. The horizontal axis of (a) is limited to the neighboring region of the pedestal top.

events by SMBI.

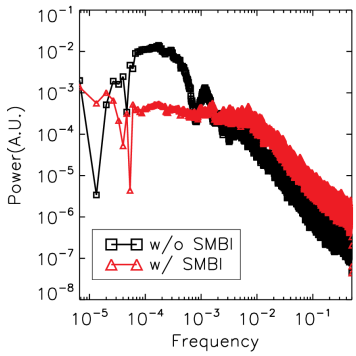

FIG. 12. The pressure fluctuation spectra at the bottom with(the red triangle) and without(the black rectangle) SMBI.

The strength and location of SMBI are varied to find an optimal injection condition to mitigate Type-I ELM. In Fig. 13, each curve shows the number of Type-I ELMs for increasing SMBI strength at a given injection location. In the bottom injection cases (the blue rectangles), Type-I ELMs disappear for the range of injection strengths $N_{inj}^{SMBI} < 15$. As the deposition location is moved inward, Type-I ELM appears as the SMBI strength increases. For the deepest injection case (the red curve), the number of Type-I ELMs increases very rapidly with the increase of injection strength. SMBIs tend to trigger Type-I ELM as does pellet pacing when the injection location is close to the pedestal top. Similar

to the cases for Type-II/III ELM mitigation by SMBI[18], we can conclude that the pedestal base is the optimal location to achieve Type-I ELM mitigation by SMBI.

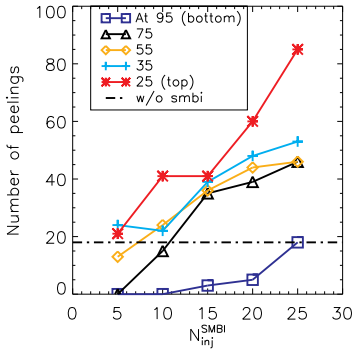

FIG. 13. The parameter scans of SMBI injection location and strength. The black dash-dotted horizontal line indicates the number of Type-I ELM events without SMBI.

V. ELM CONTROL BY PELLET INJECTION

In this section, ELM pacing by PI is studied for H-mode pedestal with Type-I ELMs. In the CA model, Type-I ELM pacing by PI works as the following. If the additional grains deposited by PI are large enough, the height of the pedestal top can reach the peeling criterion. Then, a Type-I ELM is triggered and the resulting transport removes the excessive grains from the pedestal. As will be shown in the following paragraphs, this forced Type-I ELM tends to yield smaller transports as compared to the transports by natural Type-I ELMs.

To model PI by AGI in the CA model, we choose $N_{inj}^{PI} \sim 100 N_{inj}^{SMBI}$ with shorter injection duration as in Fig. 2. The spatial profile for PI is set to take a broader form compared with the one for SMBI as Fig. 3 shows. With a relatively strong drive $N_F = 15$, Type-I ELMs appear with a period $\tau_{ELM} \sim 2600$. The duration of single PI is set as $\Delta t_{PI} = 20$. Multiple PIs are made near the pedestal top $i = 20$ with a period $T_{inj}^{PI} = 200 \sim 0.1\tau_{ELM}$.

Figure 14 shows the resulting spatio-temporal evolution of the pedestal over 25 PIs. We can immediately see that many PIs trigger Type-I ELMs immediately. However, there are also failed cases, where the injections work as fueling and lead to bigger ELMs at later times.

The time evolution on the phase space of pedestal top height and average gradient is studied to compare the cases of success and failure for ELM triggering.

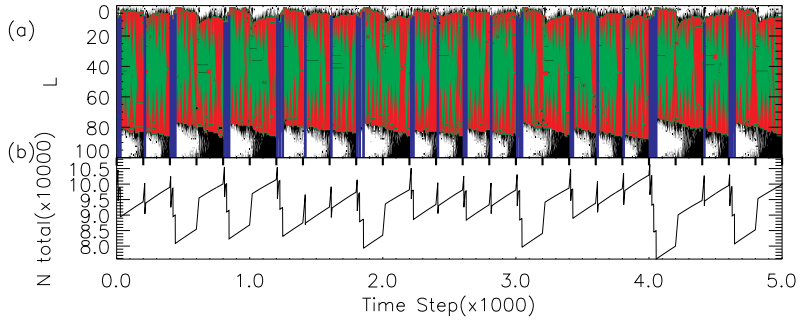

FIG. 14. The changes of the pedestal evolution by PIs. The little black solid lines at the top of the lower panel denote the pellet injection times.

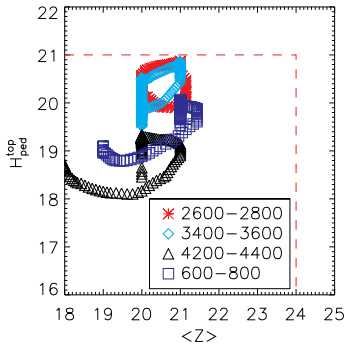

FIG. 15. The phase diagram of the pedestal gradient and height after pellet injection. The cyan and red curves denote the cases with successful forced ELM triggering. The black and blue ones correspond to failed cases.

If we plot the evolution of the pedestal top and average gradient between two PIs (see Fig. 15), it is found that the evolution follows similar circular paths, if the pellet successfully forces an ELM. However, it is important to notice that the paths followed by the successful cases do not touch the ballooning limit $\overline{Z} = 24$ (the red dashed vertical line in Fig. 15). This is because the PI period T_{inj}^{PI} is short enough to prevent the full recovery of the pedestal gradient to the limit. Also, the areas enclosed by the paths of the successful cases are smaller

than the areas of natural ELMs. This implies that smaller numbers of grains are ejected in the cases with forced-ELMs as compared with the numbers of the cases with natural ELMs.

To design an optimal scheme for pellet pacing, it is essential to find PI conditions to minimize failed cases. In this aim, we performed simulations with following sets of parameters: two different periods $T_{inj}^{PI} = 200(0.08\tau_{ELM})$ and $400(0.15\tau_{ELM})$, three different injection locations $i = 20, 30, 40$, and varying injection strengths (i.e varying number of grains). Here $i = 20$ is in the vicinity of pedestal top. Figure 16 shows the results obtained from the simulations. The colored marks in the figure indicate the number of ELM appearances divided by the number of PIs, i.e. the probability to trigger Type-I ELM. It is evident that cases of stronger (larger pellet sizes) and deeper injection (near pedestal top) have higher probability than weaker and shallower cases. Also, it is noteworthy that the pacing is more efficient for higher injection frequency case $T_{inj}^{PI} = 200$ as the rapid increase of the probability shows for the increasing injection strength with $L_c = 20$. 71% successful ELM pacing is achieved with the pellet size $N_{inj}^{PI} = 550$ for the short injection period ($T_{inj}^{PI} = 200$), while the probability drops to 56% with even bigger pellet $N_{inj}^{PI} = 600$ for the long period case ($T_{inj}^{PI} = 400$).

The key for ELM pacing experiment is maximizing PI frequency f_{PI} with the maximization of the frequency of pellet-paced ELM f_{ELM}^{P}. To investigate conditions for maximizing f_{ELM}^{P}, we performed a set of simulations with different PI frequencies $f_{PI} = 2, 3.7, 6.6, 8.8, 13.2, 17.6, 26.3 \times f_{ELM}$, different injection locations $L_c = 20, 30, 40$, and different strengths $N_{inj}^{PI} = 50 - 750$. Here f_{ELM} denotes the natural ELM frequency. The results are summarized in Fig. 17. In the figure, the horizontal axis corresponds to the PI frequency f_{PI}. Two quantities are plotted: (a) the probability to trigger Type-I ELM P_t and (b) the pellet paced ELM frequency f_{ELM}^{P}. For the perfect pellet pacing, we expect $P_t = 1$ and $f_{ELM}^{P} = f_{PI}$ (the dashed line in the Fig. 17(b)). Up to $f_{PI} < 13.2 f_{ELM}$, we obtain $f_{ELM}^{P} > 0.65 f_{PI}$ and the peak efficiency $P_t = 0.76$ is achieved at $f_{PI} = 13.2 f_{ELM}$ with $L_c = 20$. However, beyond that value, the efficiency drops as $f_{ELM}^{P} \sim 0.6 f_{PI}$ with decreasing or saturated probability $P_t \sim 0.5$.

The dropping efficiency of pellet pacing (i.e. the decrease of P_t) for increasing f_{PI} can be understood as follows. As the injection frequency increases, PI works as fueling rather than an ELM trigger. In the early phase of the recovery of the H-mode pedestal after the collapse, the total current would be still far from the peeling boundary. If PI is made during this early phase, the injection just provides additional fuel. As the injection frequency increases,

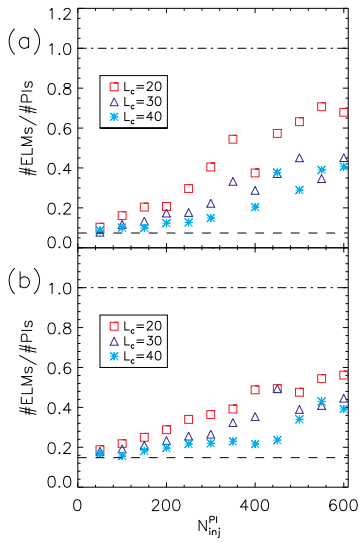

FIG. 16. The probabilities to force ELM triggering by pellets with different injection periods: (a) $T_{inj}^{PI} = 200$ and (b) $T_{inj}^{PI} = 400$. The vertical axis is the number of ELMs divided by the number of PIs. The dashed horizontal lines indicate the number of natural ELMs divided by the number of PIs

the probability of such early injections increases, and therefore the number of failed cases should increase.

We would like to note similarities between these results and the experimental trends observed in JET[21] and ASDEX-U[14]. In the experiments, a maximum achievable frequency in pellet pacing was found. Though there are many practical reasons limiting the achievable frequency, our results indicate that there can be also a fundamental limitation in the pellet pacing when the injection frequency is increased beyond a certain value. It will be an interesting future work to systematically compare the results from the CA-model and pellet pacing experiments.

VI. SUMMARY AND DISCUSSION

In this work, we extended the previous CA model to include peeling instabilities for Type-I ELM, and studied the dynamics of the H-mode pedestal with various types of ELMs. It

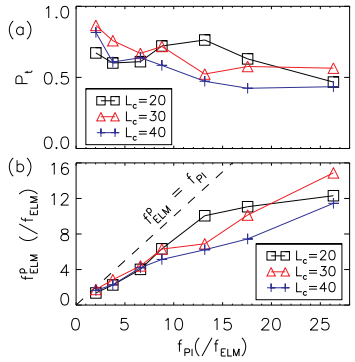

FIG. 17. (a) The probabilities and (b) frequencies of ELMs triggered by pellet injections at $L_c = 20$, 30 and 40. Pellet paced ELM frequencies are normalized by the natural ELM frequency.

was found that the extended CA model does recover the key features of the H-mode pedestal with Type-I ELMs. When the number of fueling grains N_F exceeds a certain threshold, H-mode pedestal is generated. Avalanche transport events triggered by ballooning instabilities appear and regulate the pedestal. If N_F is increased further, Type-I ELMs triggered by peeling instabilities appear periodically. The avalanche transports triggered by ballooning instabilities also appear in between the Type-I ELMs. The frequency of Type-I ELMs increases as N_F increases, which is analogues to the increase of Type-I ELM frequency in H-mode experiments with increasing input power.

SMBI and PI were modeled as AGI into the pedestal, with varying degrees of injected grains and profiles. The amount of injected materials for SMBI at one time step N_{inj}^{SMBI} was chosen to be much smaller than the values for PI N_{inj}^{PI} as $N_{inj}^{SMBI} \sim 0.01 N_{inj}^{PI}$. The total amount of injected materials over the injection time intervals are similar $N_{inj}^{SMBI}\Delta t_{SMBI} \sim N_{inj}^{PI}\Delta t_{PI}$. Also the spatial profiles for SMBI and PI were set according to their differences in penetration depth and width. Table II summarizes the differences between the ELM mitigation by SMBI and pellet pacing found from the CA modeling.

From the CA modelings of SMBI, it was found that global transport avalanches triggered by ballooning instabilities are enhanced if SMBI is applied on H-model pedestal with Type-I ELMs. The enhanced transports prevent the total current in the pedestal from reaching the peeling criterion. Then, Type-I ELMs disappear and big periodic collapses of the pedestal by the ELMs are replaced with more irregular and smaller transport events. It was noted

TABLE II. The differences between the ELM mitigation by SMBI and pellet pacing

	SMBI	**Pellet Pacing**
Injection characteristics	Shallow injection of small number of grains over long time interval	Deep injection of large number of grains over short time interval
Effects on Type-I ELM	Type-I ELMs disappear and big pedestal crashes by the ELMs are replaced with transport avalanches triggered by ballooning instabilities.	Pellet force the triggering of Type-I ELMs according to the injection frequency.
Type-I ELM control mechanism	SMBI enhances global transport avalanches triggered by ballooning instabilities, which keeps the total pedestal current and pressure below the peeling criterion.	Pellet increases the total pedestal current to reach the peeling criterion and Type-I ELM is triggered while averaged pedestal gradient is below the ballooning criterion.
Optimum injection condition	Shallow injection near the pedestal base with sufficient strength.	Deep injection near the pedestal top with sufficient strength and high frequency up to $f_{PI} \sim 13 \times f_{ELM}$.

that SMBI induces different structural changes in the distribution of transport avalanches depending on the baseline fueling N_F. If the fueling N_F is large enough to allow Type-I ELM, SMBI makes transport avalanches bigger. The resulting transport enhancement leads to the disappearance of Type-I ELM. On the other hand, if the fueling N_F is low enough to avoid Type-I ELM, SMBI enhances small scale avalanches. Then, these local avalanches regulate the pedestal from growing globally unstable to pressure gradient driven ballooning instabilities, which leads to the mitigation of Type-II/III ELMs[18].

The CA modelings of PI showed that the pellet pacing of Type-I ELM can be achieved if the injections are made with sufficient strength near the top of H-mode pedestal. If PIs successfully trigger Type-I ELMs, the height and gradient of H-mode pedestal are found to follow different evolution paths to reduce the ELM sizes from those of the natural Type-I ELMs. However, it was also found that the efficiency of pellet pacing decreases as the injection frequency increases. It is because multiple PIs can be made without proper time intervals to allow the growth of H-mode pedestal from previous collapses by Type-I ELMs. When PIs fail to trigger ELMs, they increase the pedestal pressure like additional fueling and bigger ELMs are triggered later by either PIs or spontaneous processes.

Before closing this paper, we would like to discuss the implications of our results for ELM

control experiments using SMBI and PI. In the CA model, the rules describing the transport of grains reflect all relevant physical mechanisms and processes governing the transport of H-mode pedestal. Therefore, comparing the results from CA modeling and experiment, it is essential to focus on the transport related properties, such as pressure fluctuations and their time scales etc. It will be very interesting to investigate whether the experimentally measured fluctuations and transport characteristics of H-mode pedestal show similar trends of changes by SMBI as those of the CA modeling results. In this work, it was clearly shown that the evolutions of pedestal height and gradient during natural Type-I ELMs are different from those of pellet-triggered ELMs. The differences found from the CA model can be also compared with real experiments. If the differences are confirmed, the CA modeling results can be a useful guide in designing an optimal PI scheme. Since there are great uncertainties and complexities in the very details of plasma status and operation conditions for SMBI and pellet, the optimizations of SMBI and PI require statistical approaches. We would like to emphasize that the CA model is well suited for such statistical studies.

ACKNOWLEDGMENTS

This work was supported by Korea Ministry of Science and ICT under NFRI R&D program(s) (NFRI-EN2041-6) and by CMTFO funded by the U. S. DOE Grant No. DE-FG02-04ER54738.

DATA AVAILABILITY

The data that support the findings of this study are available from the corresponding author upon reasonable request.

REFERENCES

[1]F. Wagner, Plasma Phys. Controlled Fusion **49**, B1 (2007).

[2]T. E. Evans, R. A. Moyer, P. R. Thomas, J. G. Watkins, T. H. Osborne, J. A. Boedo, E. J. Doyle, M. E. Fenstermacher, K. H. Finken, R. J. Groebner, et al., Phys. Rev. Lett. **92**, 235003 (2004).

[3]T. Evans, R. A. Moyer, K. H. Burrell, M. E. Fenstermacher, I. Joseph, A. W. Leonard,

T. H. Osborne, G. D. Porter, M. J. Schaffer, P. B. Snyder, et al., Nature Phys. **2**, 419 (2006).

[4]Y. Liang, H. R. Koslowski, P. R. Thomas, E. Nardon, B. Alper, P. Andrew, Y. Andrew, G. Arnoux, Y. Baranov, M. Bécoulet, et al., Phys. Rev. Lett. **98**, 265004 (2007).

[5]W. Suttrop, T. Eich, J. C. Fuchs, S. Günter, A. Janzer, A. Herrmann, A. Kallenbach, P. T. Lang, T. Lunt, M. Maraschek, et al., Phys. Rev. Lett. **106**, 225004 (2011).

[6]T. Hender, R. Fitzpatrick, A. Morris, P. Carolan, R. Durst, T. Edlington, J. Ferreira, S. Fielding, P. Haynes, J. Hugill, et al., Nuclear Fusion **32**, 2091 (1992).

[7]W. Xiao, P. Diamond, X. Zou, J. Dong, X. Ding, L. Yao, B. Feng, C. Chen, W. Zhong, M. Xu, et al., Nucl. Fusion **52**, 114027 (2012).

[8]W. Xiao, P. Diamond, W. Kim, L. Yao, S. Yoon, X. Ding, S. Hahn, J. Kim, M. Xu, C. Chen, et al., Nuclear Fusion **54**, 023003 (2014).

[9]Z. C. Yang, Z. B. Shi, W. L. Zhong, B. Y. Zhang, Q. C. Fan, H. D. Li, M. Jiang, P. W. Shi, C. Y. Chen, W. Chen, et al., Physics of Plasmas **23**, 012515 (2016), https://doi.org/10.1063/1.4940940, URL `https://doi.org/10.1063/1.4940940`.

[10]J. Kim, Y.-M. Jeon, W. Xiao, S.-W. Yoon, J.-K. Park, G. Yun, J.-W. Ahn, H. Kim, H.-L. Yang, H. Kim, et al., Nuclear Fusion **52**, 114001 (2012).

[11]B. Wan, J. Li, H. Guo, Y. Liang, G. Xu, L. Wang, and X. G. and, Nuclear Fusion **55**, 104015 (2015).

[12]P. Lang, J. Neuhauser, L. Horton, T. Eich, L. Fattorini, J. Fuchs, O. Gehre, A. Herrmann, P. Ignácz, M. Jakobi, et al., Nuclear Fusion **43**, 1110 (2003).

[13]P. Lang, G. Conway, T. Eich, L. Fattorini, O. Gruber, S. Günter, L. Horton, S. Kalvin, A. Kallenbach, M. Kaufmann, et al., Nuclear Fusion **44**, 665 (2004).

[14]P. Lang, A. Burckhart, M. Bernert, L. Casali, R. Fischer, O. Kardaun, G. Kocsis, M. Maraschek, A. Mlynek, B. Plöckl, et al., Nuclear Fusion **54**, 083009 (2014), URL `https://doi.org/10.1088%2F0029-5515%2F54%2F8%2F083009`.

[15]L. R. Baylor, N. Commaux, T. C. Jernigan, N. H. Brooks, S. K. Combs, T. E. Evans, M. E. Fenstermacher, R. C. Isler, C. J. Lasnier, S. J. Meitner, et al., Phys. Rev. Lett. **110**, 245001 (2013).

[16]I. Gruzinov, P. H. Diamond, and M. N. Rosenbluth, Phys. Rev. Lett. **89**, 25 (2002).

[17]I. Gruzinov, P. H. Diamond, and M. N. Rosenbluth, Phys. Plasmas **10**, 569 (2003).

[18]T. Rhee, J. M. Kwon, P. H. Diamond, and W. W. Xiao, Phys. Plasmas **19**, 022505 (2012).

[19]H. Wilson, Fusion Sci. Technol. **53**, 161 (53).

[20]G. T. A. Huysmans, S. Pamela, E. van der Plas, and P. Ramet, Plasma Physics and Controlled Fusion **51**, 124012 (2009), URL https://doi.org/10.1088%2F0741-3335%2F51%2F12%2F124012.

[21]P. Lang, A. Alonso, B. Alper, E. Belonohy, A. Boboc, S. Devaux, T. Eich, D. Frigione, K. Gál, L. Garzotti, et al., Nuclear Fusion **51**, 033010 (2011).

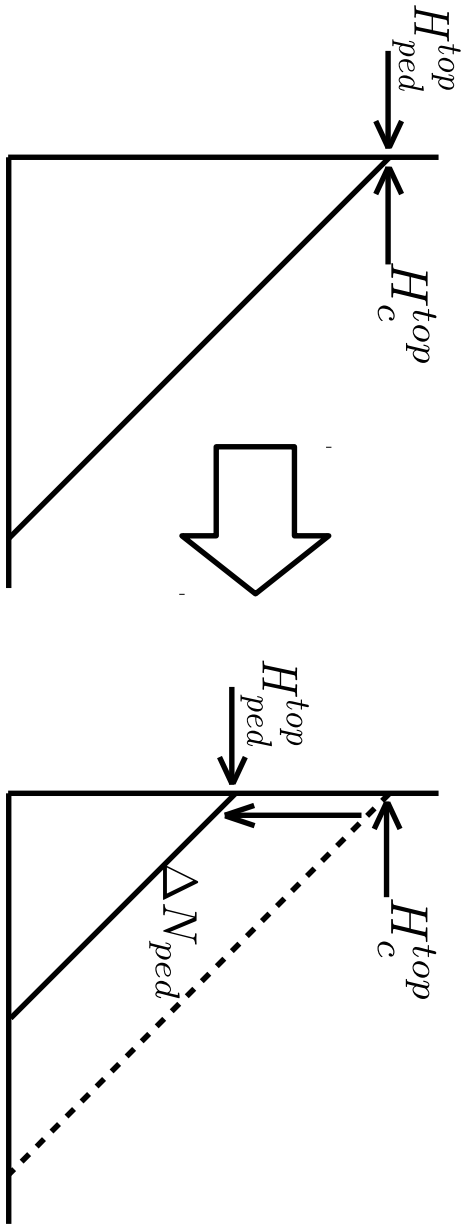

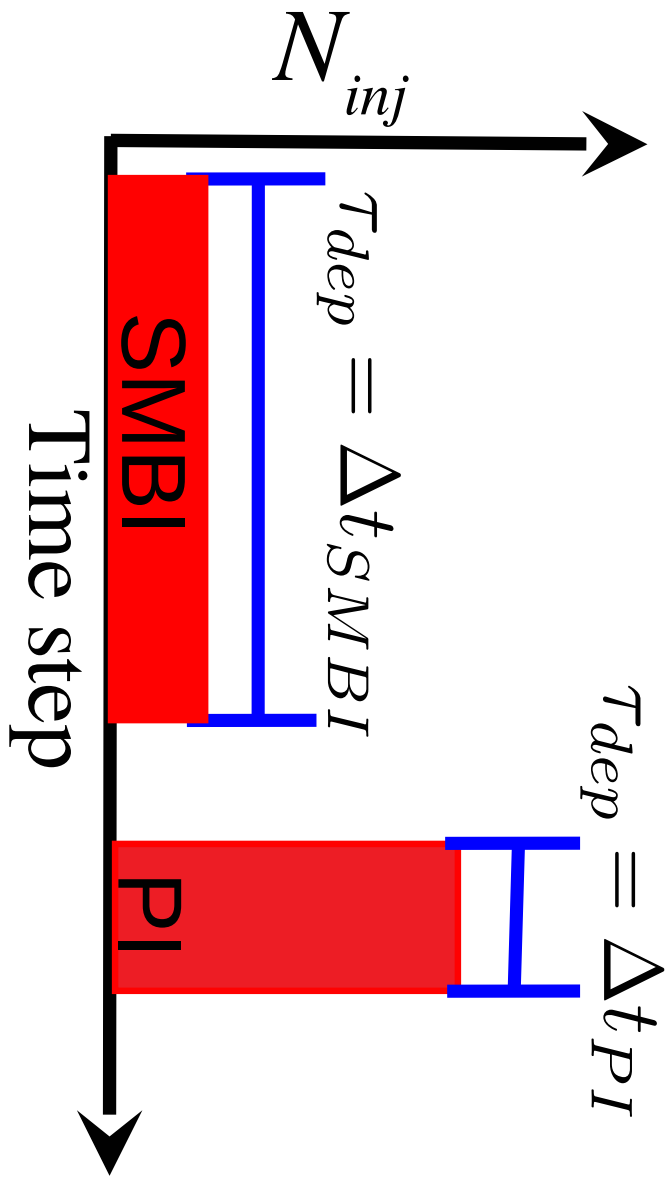

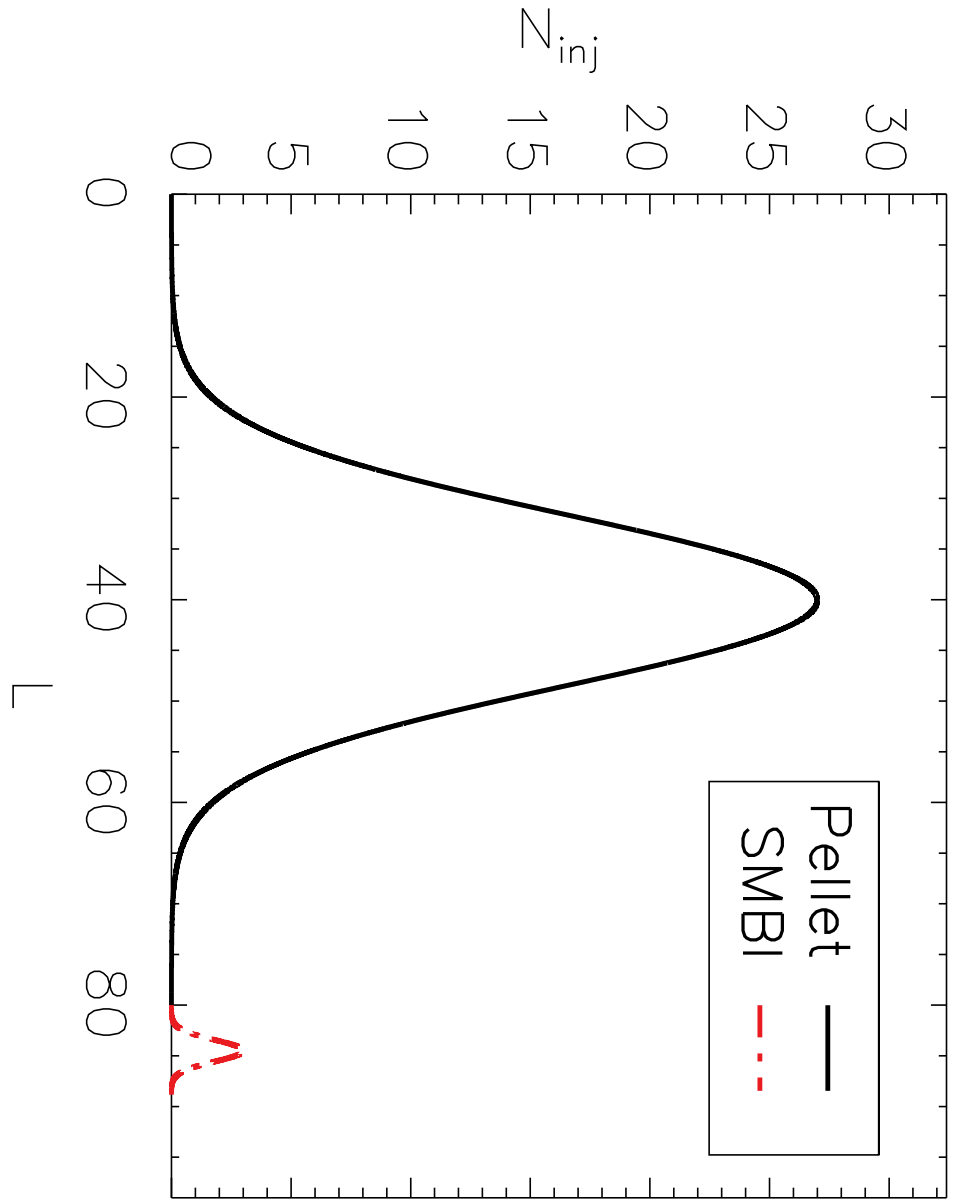

PLEASE CITE THIS ARTICLE AS DOI: 10.1063/5.0009583

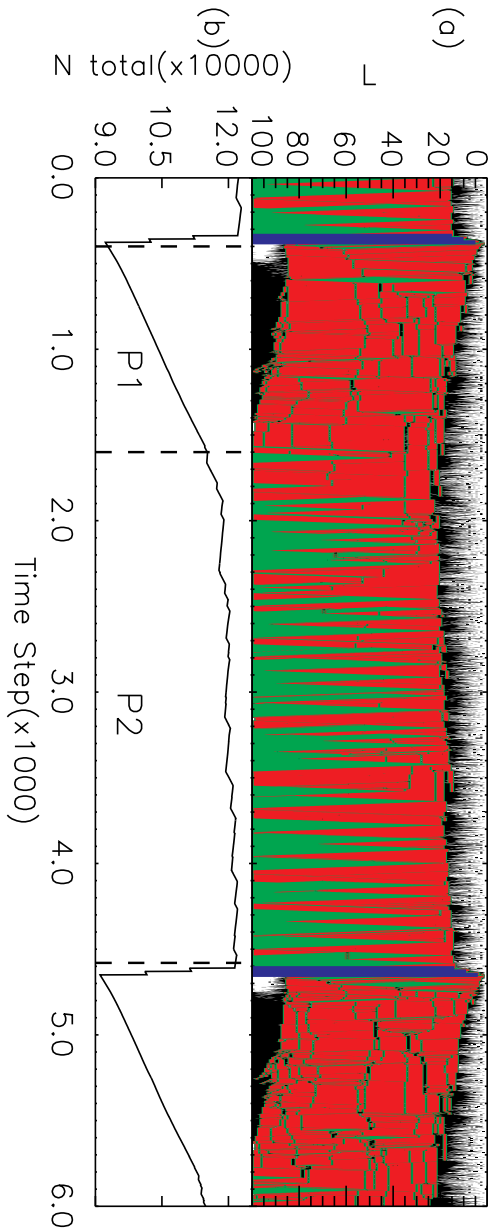

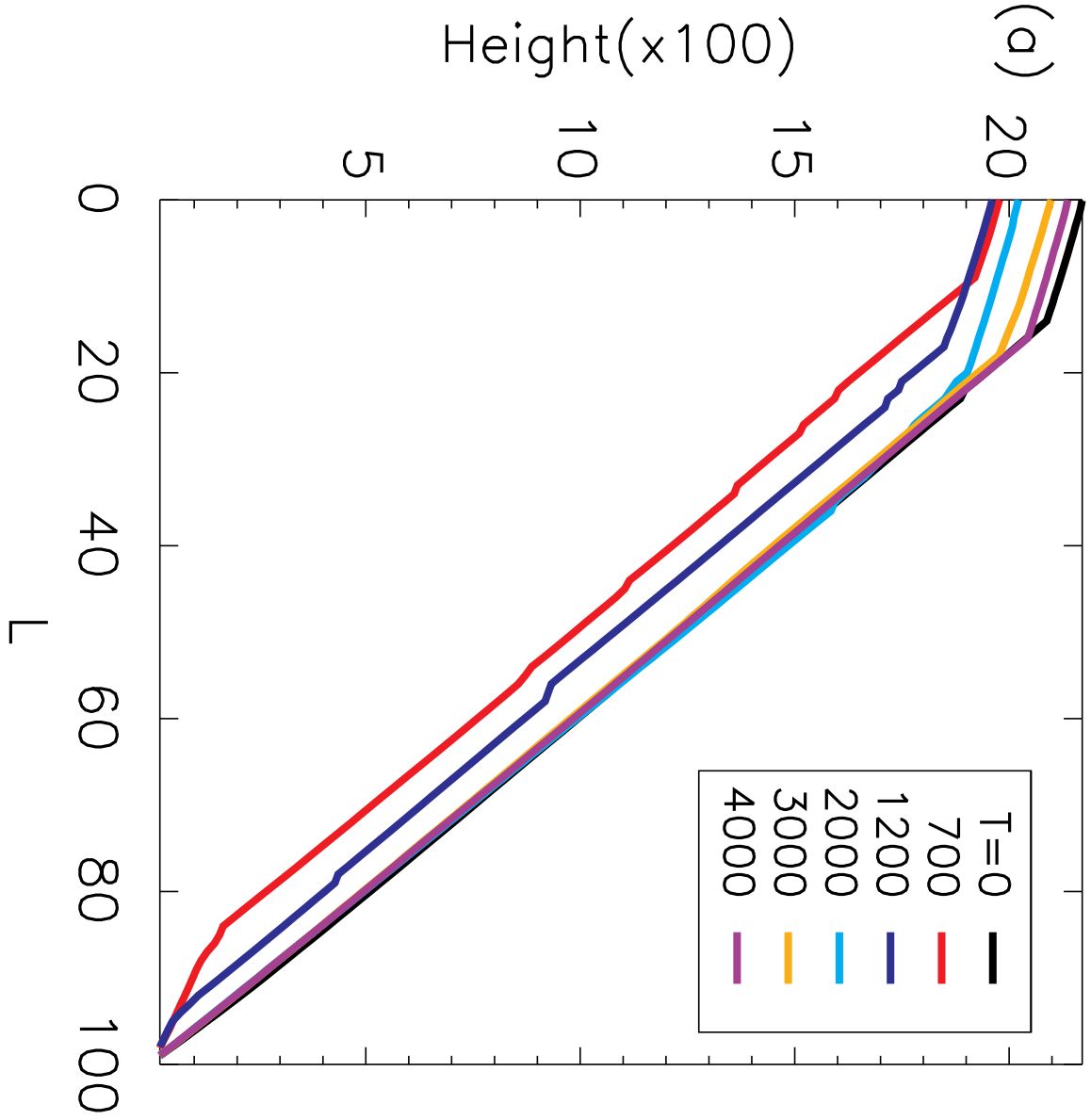

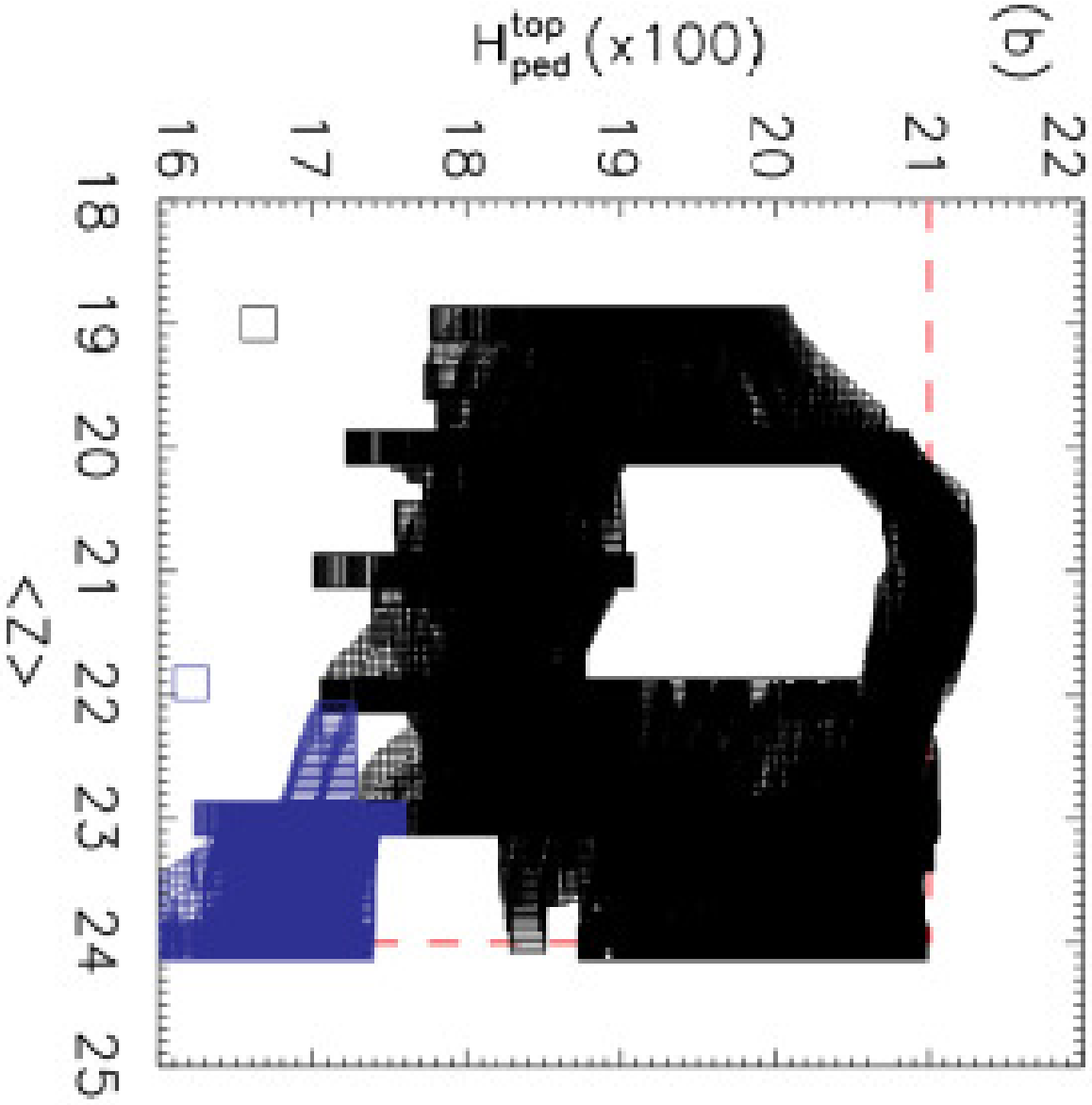

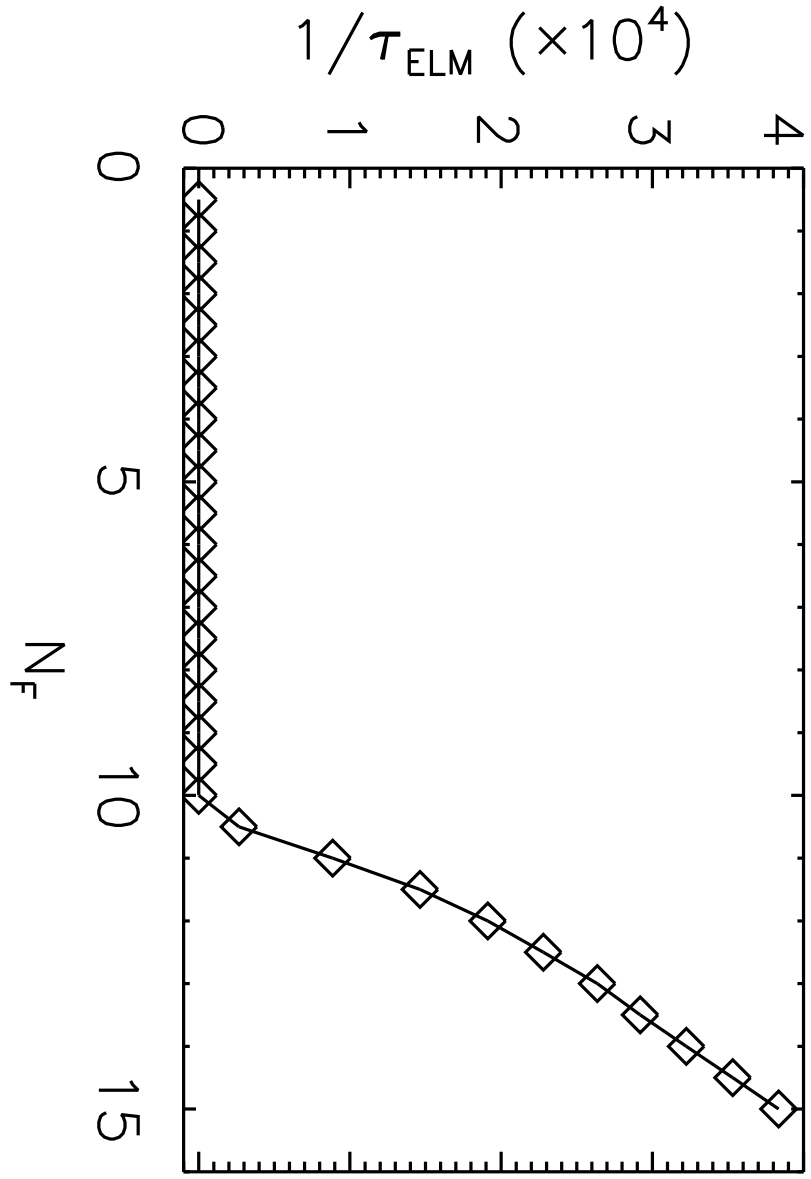

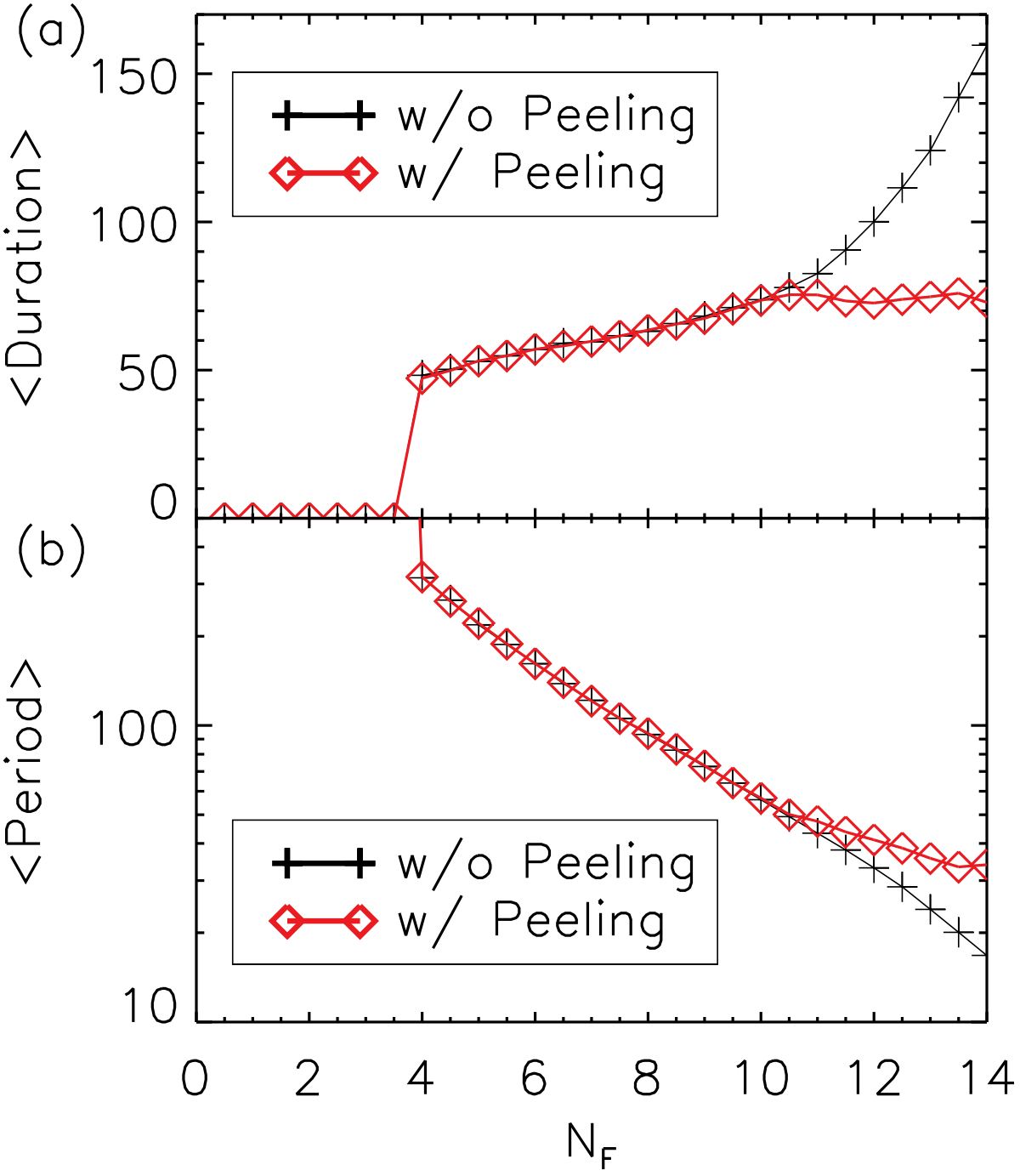

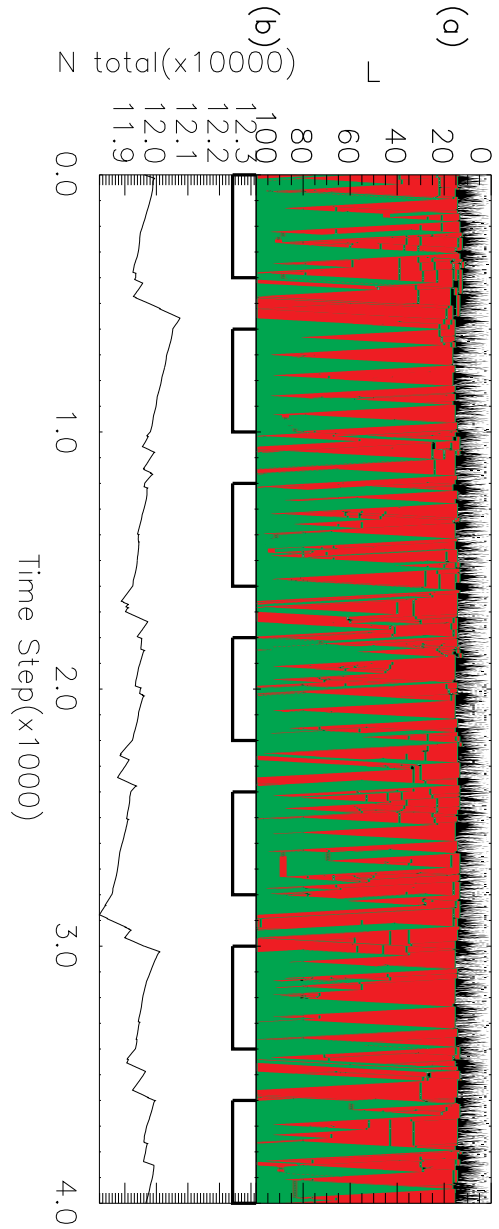

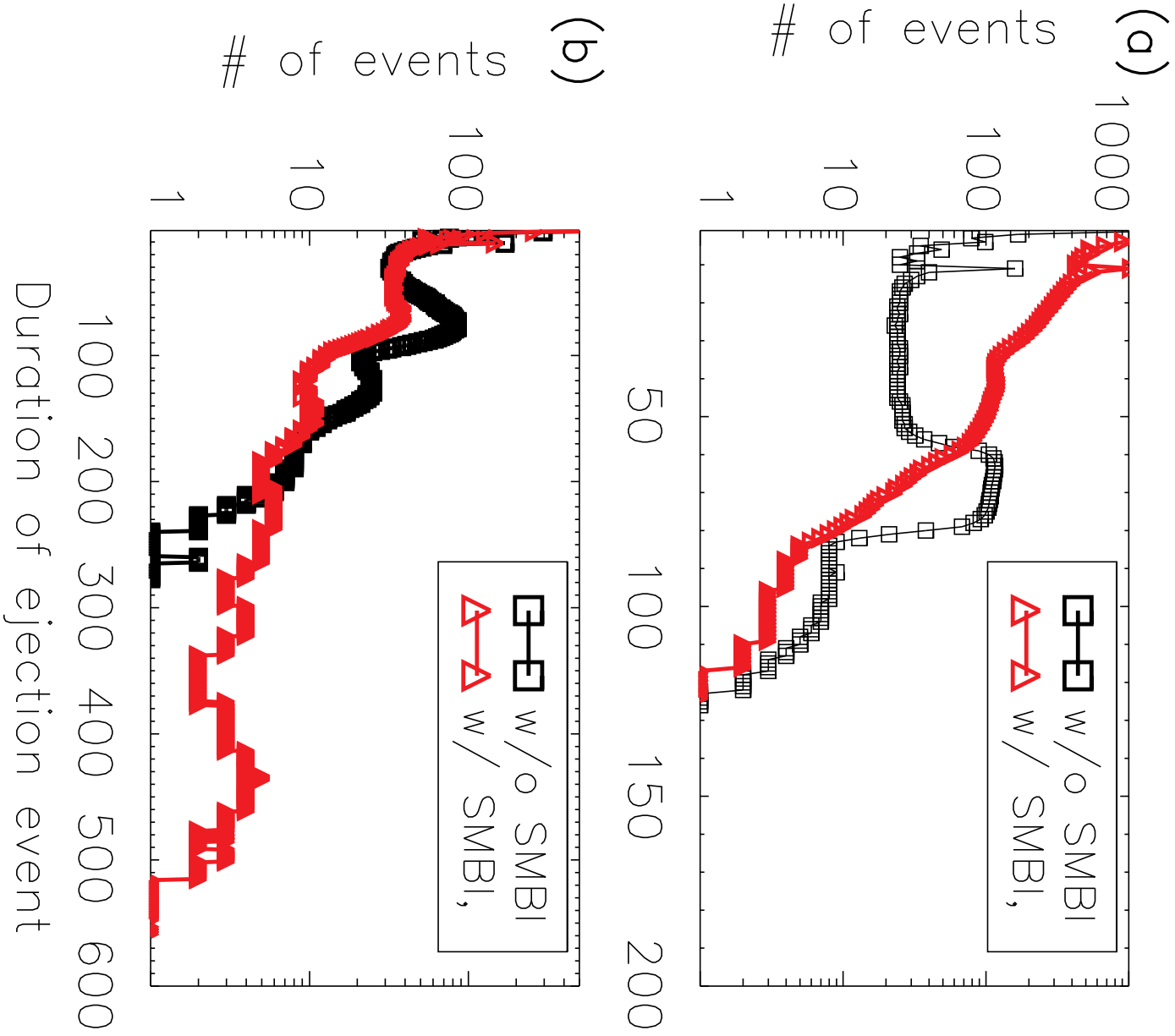

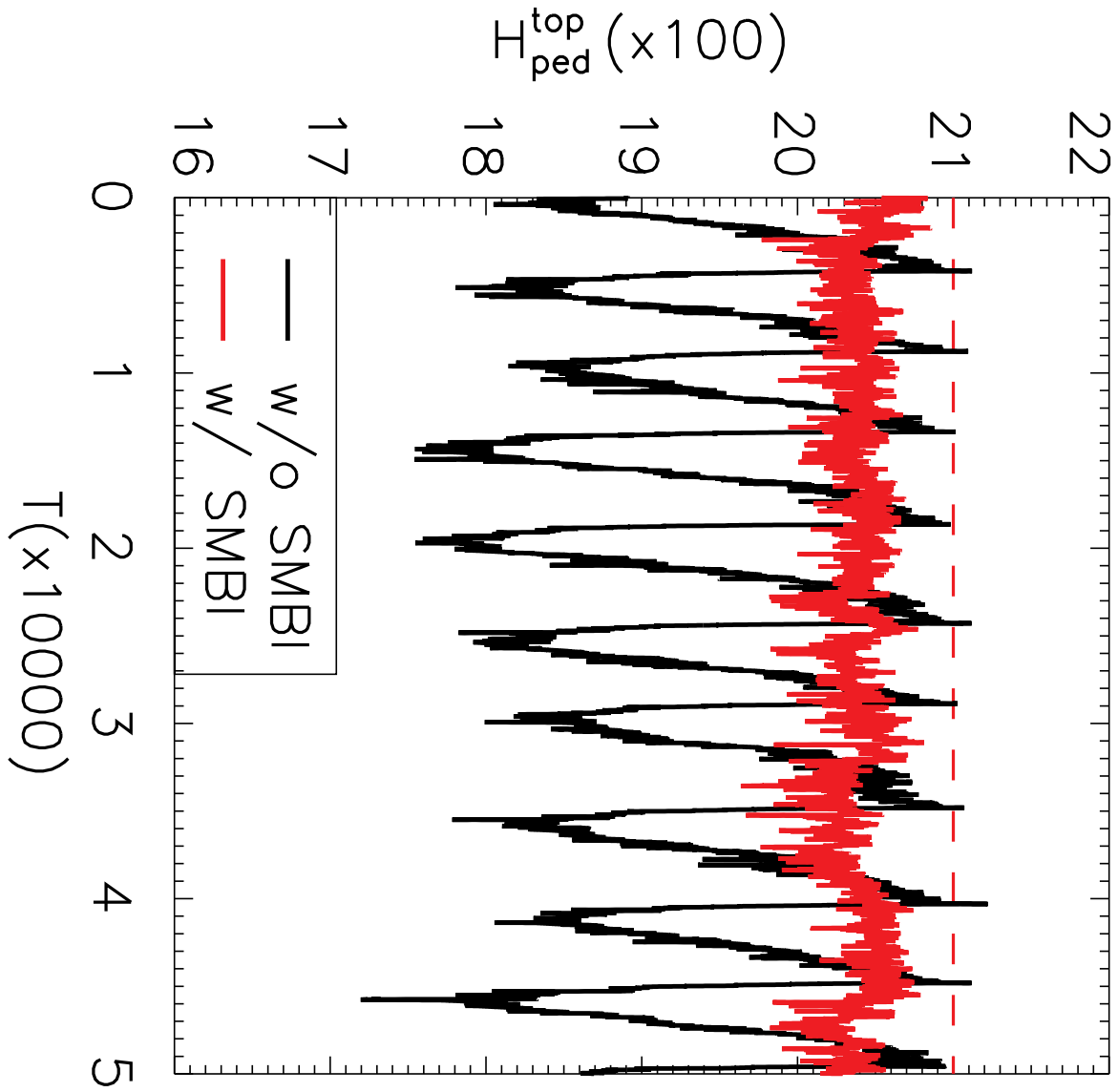

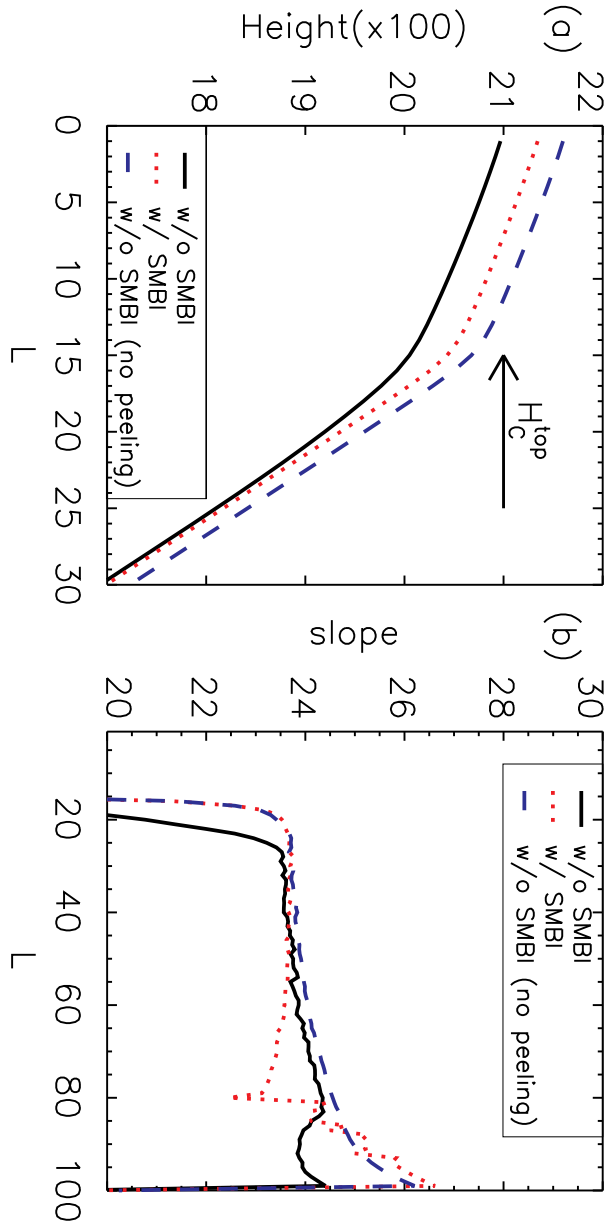

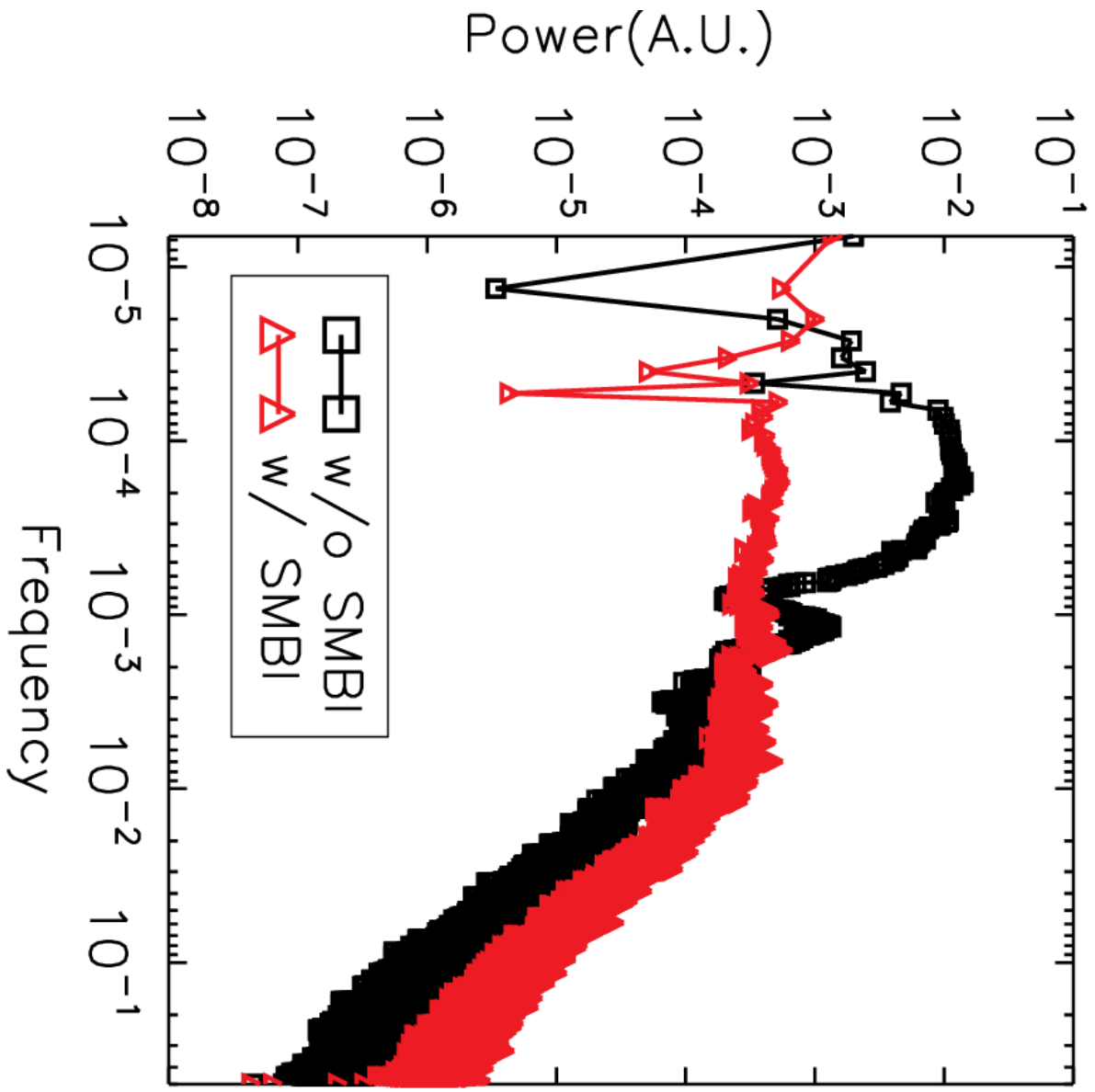

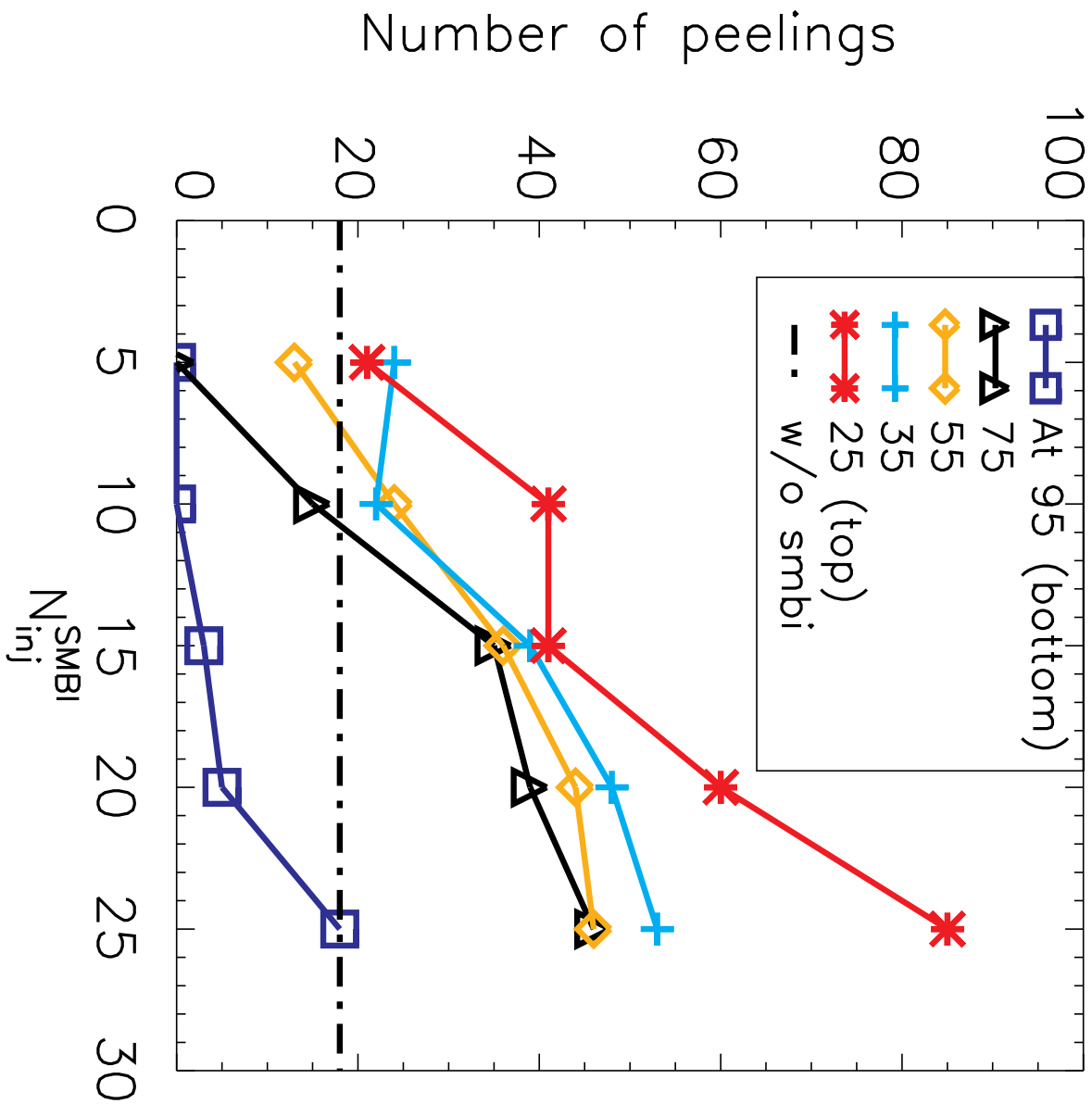

PLEASE CITE THIS ARTICLE AS DOI: 10.1063/5.0009583